Article

Effects of the Pore Structure and Acid−Base Property of X Zeolites on Side-Chain Alkylation of Toluene with Methanol

He Han, Min Liu,* Hong Yang,* Chuan Shi, Shutao Xu, Yingxu Wei, Zhongmin Liu, Chunshan Song, and Xinwen Guo*

Read Online

ACCESS | Metrics & More | Article Recommendations | Supporting Information

ABSTRACT: One of the potential processes for making styrene monomers is side-chain alkylation of toluene with methanol, and X zeolites (a common type of faujasite) have been identified as one of the most suitable catalysts for this reaction. In this work, a series of X zeolites with different micro- and meso-porosities and acid−base properties are prepared by post-treatments of NaX zeolite and their catalytic performances for the side-chain alkylation of toluene with methanol are evaluated. This study shows that intracrystalline mesopores could be introduced into the NaX zeolite while retaining adequate microporosity through controlling the intensity and sequence of ammonium-exchange (AE) and/or dealumination (DA) post-treatments. The loss in basicity of the resulting mesoporous X zeolites due to AE and/or DA treatments could be compensated and even enhanced by the subsequent cesium modifications. As catalysts for the side-chain alkylation reaction, the study shows that while introducing appropriate mesopores into X zeolites enhances molecular diffusion, the restriction effect of micropores is proven to be critical for their catalytic activity. Moreover, it is the acid−base property rather than the pore structure of the post-treated X zeolites determining their catalytic activity and selectivity for the side-chain alkylation reaction.

Effects of the pore structure and acid-base property of X zeolites on side-chain alkylation of toluene with methanol
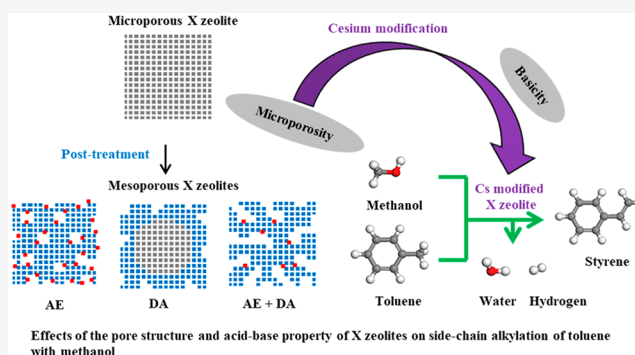
1. INTRODUCTION

Styrene is an important chemical for the production of polystyrene, styrene−butadiene rubber, and other industrial plastics.[1] The classical route for a large-scale styrene production is based on a gas-phase or liquid-phase alkylation reaction, typically starting from benzene alkylation with ethylene using zeolite catalysts (e.g., ZSM-5, Y, MCM-22, Beta, etc.), followed by the dehydrogenation of ethyl-benzene.[2−4] One of the most widely investigated alternative routes for styrene synthesis is the side-chain alkylation of toluene with methanol.[5−7] This process has the advantages of low-cost raw materials, low reaction temperature, and lower energy consumption compared to the traditional Friedel−Crafts alkylation of benzene with ethylene.[8−14] The side-chain alkylation of toluene with methanol is typically catalyzed by microporous X and Y zeolites, both belonging to the faujasite (FAU) family. The catalytic performance of K and Rb ion-exchanged X zeolites for this reaction was first reported by Sidorenko et al.[8] in as early as 1967. Subsequently, most of the reported work,[15−17] including our own work,[18,19] has mainly focused on investigating the catalytic performance of alkali metal modified microporous X or Y zeolites.

It is well recognized that FAU-type topology structure is indispensable for the side-chain alkylation of toluene with methanol.[10,12] The basicity inherent to this topology dictates the catalytic activity. However, the micropore structure within the FAU topology limits the diffusion of the reactant/product molecules and accessibility of active sites.[6,20] It is recognized to be responsible for the low conversion of toluene as well as unsatisfactory styrene selectivity of side-chain alkylation of toluene.[21]

To improve the catalytic performance of FAU zeolites, various approaches have been trialed and reported aiming at altering the pore structure of these zeolites, including ball milling[10,20,22] and creation of hierarchical mesopore and macropores.[23−25]

Ball milling is a physical process. It can effectively fracture bulky FAU particles into much smaller fragments and in doing so create new external surfaces and enhance the accessibility of the active sites. The work by Xie et al.[22] and Liu et al.[20] both showed that controlled ball milling of X zeolites could enhance the catalytic performance of the zeolites and improve the yield of styrene and ethylbenzene during the alkylation. However,

ball milling is also a destructive process. Excessive ball milling will destroy the topological structure of FAU zeolites and thus diminish the active sites in these zeolites. This has been demonstrated by the work carried out by Wieland et al.[10] on the effect of ball milling on Y zeolites. It showed that ball milling of bulky Y zeolite particles can drastically reduce the micropore volume of the zeolite and diminished its catalytic activity.

The other strategy to alter pore structure of FAU zeolites is to introduce hierarchical meso- and macro-pores within the intrinsic microporous topological structure.[26] Among various routes to achieve this, post chemical treatment of conventional microporous X zeolite crystals gain most of the traction due to its versatility and simplicity in operation.[24] For example, Lee et al.[25] reported that controlled decationization via ammonium-exchange of NaX zeolite could produce hierarchically X zeolites with adjustable micro- and meso-porosity. Verboekend et al.[23] also showed that a mild dealumination of ammonium-exchanged NaX with ethylenediamine-tetraacetic acid disodium salt dehydrate (Na_2H_2EDTA) would also increase the mesoporosity. It is, however, important to recognize that any chemical process will inevitably also alter the chemical nature of the zeolites, thus impacting the nature of the active sites. This means systematic work are often required to optimize the catalytic performance of the mesoporous zeolites produced by chemical post-treatments.

The aim of this work is to develop a chemical post-treatment strategy to optimize the pore structure and basicity property of X zeolites for the side-chain alkylation of toluene with methanol. In the study, a series of X zeolites with different micro- and meso-porosities were prepared by ammonium-exchange (AE), dealumination (DA), and combined AE+DA methods. The catalytic performances over these X zeolites for the side-chain alkylation of toluene with methanol were investigated. In addition, the catalytic performance is correlated to the pore structure and acid−base property of the specific zeolite.

2. EXPERIMENTAL SECTION

2.1. Chemicals and Materials. NaX zeolite (SiO_2/Al_2O_3 = 2.5) is obtained from the Catalyst Plant of Nankai University. Ammonium nitrate (NH_4NO_3, 99.9%) and Na_2H_2EDTA (99.9%) were obtained from Sinopharm Chemical Reagent Co., Ltd. Cesium nitrate ($CsNO_3$, 99.0%) and cesium hydroxide monohydrate ($CsOH\cdot H_2O$, 99.9%) were obtained from Aladdin Industrial Corporation.

2.2. Catalyst Preparation. Three methods were employed to prepare mesoporous X zeolites, including the ammonium-exchange (AE), dealumination (DA), and combined AE+DA.[23,25]

In AE treatment, the parent NaX zeolite was ion-exchanged in NH_4NO_3 solutions of varied concentrations from 0.025 to 0.4 M. The ion-exchange was always repeated three times at 343 K for 2 h using the same solid/liquid ratio of 10 g/50 mL. Each time, the exchanged solid was isolated by centrifugation and washed with excess deionized water. After the AE process, the solid sample was dried at 373 K for 12 h and finally calcined at 773 K for 2 h. The samples so-obtained are named as AE1, AE2, AE3, AE4, AE5, and AE6, corresponding to the NH_4NO_3 concentrations used in the treatment, namely 0.025, 0.05, 0.1, 0.2, 0.4, and 0.8 M, respectively.

In DA treatment, parent NaX zeolite was treated in Na_2H_2EDTA solutions of varied concentrations from 0.1 to 0.3 M at a solid/liquid ratio of 10 g/20 mL and stirred at 368 K for 6 h. The treated sample was then recovered, washed, dried, and calcined following the same procedures as for the AE samples. The resulted samples are named as DA1, DA2, DA3, and DA4, corresponding to the 0.1, 0.15, 0.2, and 0.3 M of Na_2H_2EDTA treatment solution, respectively.

Finally, parent NaX zeolite was subjected to combined AE +DA sequential treatments, and the resulting samples are named as AE1+DA1, AE1+DA3, AE3+DA1, AE3+DA3, AE5+DA1, and AE5+DA3, respectively, according to the detailed treatments to which it is being subjected. For example, the AE3+DA3 refers to the sample produced from NaX zeolite which was first ion-exchanged in the 0.1 M NH_4NO_3 solution, isolated, dried and calcined, and then dealuminated in the 0.2 M Na_2H_2EDTA solution followed again with the isolation, drying, and calcination.

To investigate the catalytic performance of the prepared NaX zeolites for side-chain alkylation of toluene with methanol, cesium ion-exchange (CE) and subsequent cesium impregnation (CE+CI) were carried out to enhance the basicity of these X zeolites. In a typical cesium ion-exchange, a mesoporous NaX sample was first ion-exchanged in 0.2 M $CsNO_3$ solution (solid/liquid ratio, 10 g/20 mL) at 343 K for 2 h for three times. The ion-exchanged sample was then isolated, dried, and calcined at 813 K for 3 h. The resulting sample is then named with CE subscript, i.e., AE_{CE}, DA_{CE}, and $(AE+DA)_{CE}$. Finally, the CE samples were further modified with CsOH solution by incipient wetness impregnation. The loading of Cs_2O was controlled at 10 wt % following a previously established procedure.[19] The resulted samples are named with CE+IC subscript, i.e., AE_{CE+CI}, DA_{CE+CI}, and $(AE+DA)_{CE+CI}$. Note that the cesium ion-exchanged parent NaX is named NaX_{CE}. When it is being further modified by cesium impregnation, it is named NaX_{CE+CI}.

2.3. Characterization. Powder X-ray diffraction (XRD) patterns were recorded on a Rigaku SmartLab diffractometer with a Cu Kα radiation source operating at 45 kV and 200 mA. The spectra were recorded from 5° to 50° with a step size of 0.02° and a scanning rate of 8° min^{-1}. XRD samples were prepared using a same sample holder packed with almost identical mass of each sample. The relative crystallinity (RC) of each sample was determined from the peak areas of 2θ = 6.2° [111], 2θ = 15.6° [331], and 2θ = 23.2° [533] using parent NaX as a reference (RC = 100%) following a reported method.[27]

Scanning electron microscopy (SEM) images were obtained on a field-emission scanning electron microscopy (NOVA NanoSEM 450) at an acceleration voltage of 10.0 kV. All the SEM samples were sputtered with a thin film of chromium for conductivity.

Transmission electron microscopy (TEM) images were taken on a Tecnai G2 20 S-twin instrument (FEI Company) at an acceleration voltage of 200 kV. The samples for TEM analysis were prepared by dipping the carbon-coated copper grids into an ethanol solution of the sample and allowed to dry under ambient conditions.

N_2 adsorption/desorption isotherms were measured using a Quantachrome autosorb-iQ2 gas adsorption analyzer at 77 K. Prior to the measurement, the samples were degassed in vacuum at 573 K for 10 h. The t-plot method was used to discriminate between micro- and meso-porosity. The reported mesopore volumes (V_{meso}) consist of contributions from the intercrystalline mesopores as well as intracrystalline mesopores

of the particles. Mesopore size distribution curves of the samples were obtained by the BJH method.

Argon isotherms were measured using a Quantachrome AUTOSURB-1 gas adsorption analyzer at 87 K to determine the BET surface area and micropore pore volume. Pore size distribution curves were obtained by the NLDFT method.

The SiO_2/Al_2O_3 ratios of the zeolite samples were determined by the X-ray fluorescence (XRF) spectroscopy on a Philips Magix-601 X-ray fluorometer. The XRF sample was prepared by first mixing 0.5 g zeolite with 8.5 g anhydrous lithium tetraborate and lithium metaborate. The mixed powder was then transferred to a platinum crucible and heated to 1000 °C to form a molten salt. After allowing to cool down to room temperature, the molten liquid solidified into a disc of ~5 mm in thickness. This transparent disc is used for the XRF measurement.

X-ray photoelectron spectroscopy (XPS) measurements were performed on Escalab 250 (Thermo Fisher VG). The based pressure was 2.4×10^{-8} Pa. Monochromatized Al Kα 1486.6 eV radiation was used as the X-ray source. The binding energies were referenced to the C 1s band at 284.6 eV. Cleaning of the sample surface was performed by Ar$^+$ ion sputtering followed by annealing in vacuum.

^{29}Si and ^{27}Al magic angle spinning nuclear magnetic resonance (MAS NMR) measurements were performed on a 600 MHz Bruker Avance III spectrometer equipped with a 4 nm MAS probe. ^{29}Si MAS NMR spectra were recorded using high-power proton decoupling with a spinning rate of 10 kHz. With a $\pi/2$ pulse width of 3 μs and a 10 s recycle delay 1024 scans were accumulated. The chemical shifts were referenced to DSS (4,4-dimethyl-4-silapentanesulfonate sodium) at 0 ppm. ^{27}Al MAS NMR spectra were recorded using one pulse sequence with a spinning rate of 12 kHz. With a $\pi/8$ pulse width of 0.75 μs and a 2 s recycle delay 100 scans were performed. The chemical shifts were referenced to (NH$_4$)Al-(SO$_4$)$_2$.12H$_2$O at -0.4 ppm. The software Dmfit was employed for deconvolution using fitting of the Gaussian–Lorentzian lineshapes.

Fourier transform infrared (FT-IR) spectra of the zeolite skeleton were recorded from 4000 to 400 cm^{-1} on an EQUINOX55 FT-IR spectrometer (Bruker Corp.) with a resolution of 4 cm^{-1}, and the KBr pellet technique was adopted.

Temperature-programmed desorption (TPD) of NH$_3$ and CO$_2$ were performed on a CHEMBET 3000 chemical adsorber (Quantachrome, USA) to analyze the nature of surface acidic and basic sites. In a typical NH$_3$-TPD measurement, about 0.1 g of the sample was degassed in helium at 773 K for 1 h, cooled to 393 K, and then exposed to an ammonia-helium mixture (8% NH$_3$-92% He) for 30 min. The physically adsorbed NH$_3$ was removed by helium at 393 K for 1 h. The TPD curves were obtained at a heating rate of 10 K min^{-1} from 393 to 923 K. The desorbed ammonia was detected by gas chromatography equipped with a thermal conductivity detector. The CO$_2$-TPD measurements were conducted under mostly the same conditions as in the NH$_3$-TPD, except the absorption gas was pure CO$_2$, and the degassed samples were cooled to 303 K for the subsequent absorption and desorption of CO$_2$.

2.4. Catalytic Testing. Side-chain alkylation of toluene (T) with methanol (M) was carried out at atmospheric pressure in a fixed bed, vertical, down-flow stainless steel reactor placed inside a tube furnace. N$_2$ was used as a carrier gas at a molar ratio of N$_2$/(T+M) = 2. About 1.6 g of the

catalyst was employed in the test. Prior to the reaction, the catalyst was sieved to 10−20 mesh particle sizes, pretreated *in situ* at 773 K for 1.5 h under flowing N$_2$, and then cooled down to the reaction temperature set at 698 K. The mixture of toluene and methanol with a molar ratio of T/M = 6 was fed into the reactor using an injection pump at a weight hourly space velocity (WHSV) of 2.0 h^{-1}. The gaseous effluent from the reactor was collected in a cold trap at 273 K. The liquid products were analyzed in a gas chromatograph (Agilent Technologies GC6890) equipped with an INNOWAX capillary column (60 m length, inner diameter 0.25 mm, stationary phase thickness 0.25 μm) and a flame ionization detector (FID). Gaseous products were analyzed in another gas chromatograph (Tianmei GC 7890F) equipped with a HayeSep Q packed column (2 m length, inner diameter 2 mm) and a FID. The gaseous products passed through a methanization converter filled with Ni catalyst to convert carbon oxide products to methane before they went to the FID to ensure a high signal intensity.

The conversion of toluene (C_T), selectivity of styrene (S_{ST}), total selectivity of styrene and ethylbenzene (S_{ST+EB}), yield of styrene (Y_{ST}), and total yield of styrene and ethylbenzene (Y_{ST+EB}) are defined in the following equations:

$$C_T(\%) = \left(1 - \frac{[\text{toluene outlet}]}{[\text{toluene inlet}]}\right) \times 100\% \tag{1}$$

$$S_{ST}(\%) = \left(\frac{[\text{styrene}]}{[\text{tolune inlet}] - [\text{toluene outlet}]}\right) \times 100\% \tag{2}$$

$$S_{ST+EB}(\%) = \left(\frac{[\text{styrene}] + [\text{ethylbenzene}]}{[\text{tolune inlet}] - [\text{toluene outlet}]}\right) \times 100\% \tag{3}$$

$$Y_{ST}(\%) = C_T \times S_{ST} \tag{4}$$

$$Y_{ST+EB}(\%) = C_T \times S_{ST+EB} \tag{5}$$

The reaction rate and turn over frequency (*TOF*) of side-chain alkylation of toluene with methanol to styrene and ethylbenzene are defined in the following equations:

$$\text{reaction rate} = \frac{[\text{styrene and ethylbenzene}]}{\text{mass of catalyst} \times \text{unit time}} \tag{6}$$

$$TOF = \frac{\text{reaction rate of toluene to styrene and ethylbenzene}}{\text{base density of CsNaX}} \tag{7}$$

3. RESULTS AND DISCUSSION

3.1. Effects of Different Post-Treatment on the X Zeolites. *3.1.1. Structure Characterization of Post-Treated X Zeolites.* Figure 1 shows the XRD patterns of parent NaX and three series of post-treated zeolite samples. As seen, NaX exhibits a diffraction pattern of a typical highly crystalline faujasite structure.[25,28] It is also evident that post-treatments do not change the overall FAU structure of the resulting samples.

However, as seen in Figure 1A for AE samples, the intensities of characteristic diffraction peaks decrease progressively with the increased intensity of the AE treatment (i.e., increased NH$_4$NO$_3$ concentration). The relative crystallinity (RC) values of AE samples are estimated and their values provided in Table 1 and Table S1. Clearly, the relative
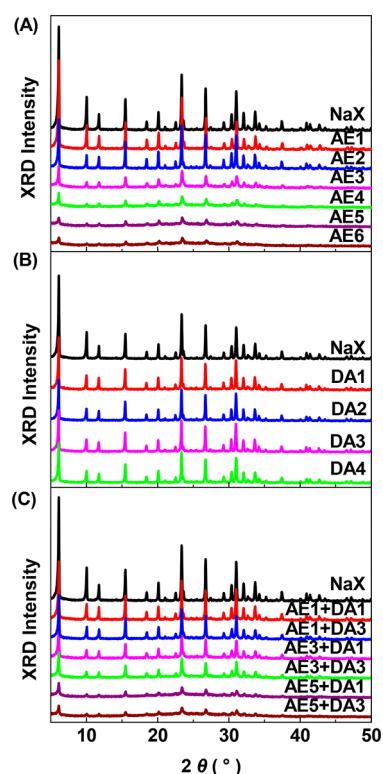
Figure 1. XRD patterns of parent NaX zeolite and post-treated samples. (A) ammonium-exchange (AE), (B) dealumination (DA), and (C) the combination of ammonium-exchange and dealumination (AE+DA).

crystallinity decreases dramatically from 82% (AE1) to 7% (AE6) with the progressively intensified AE treatment. In contrast, as seen in Figure 1B, the XRD intensities for DA samples do not change as significantly with intensified DA treatment; the relative crystallinity of DA samples is found to range from ~72% (DA1) to 61% (DA4). Again, the RC values for DA samples are also provided in Table 1 and Table S1.

As expected, when the parent NaX zeolite is subjected to AE +DA treatments as observed in Figure 1C, the resulting samples display RC values ranging from ~65% (AE1+DA1) to 10% (AE5+DA3). Notably, the RC values of AE1+DA1(65%) and AE1+DA3(49%) are lower than that of AE1(82%), while the RC values of AE3+DA1(37%) and AE3+DA3(29%) are

higher than that of AE3(24%). This indicates that DA treatments could either decrease or increase relative crystallinity of the resulting X zeolite, depending on the physicochemical state of the X zeolite before the treatment. It is worth noting that the combination AE+DA enables some degree of control and adjustment of crystallinity in treated X zeolites.

Figure 2 shows the SEM and TEM images of the parent NaX and AE3, DA3, and AE3+DA3 post-treated samples. The
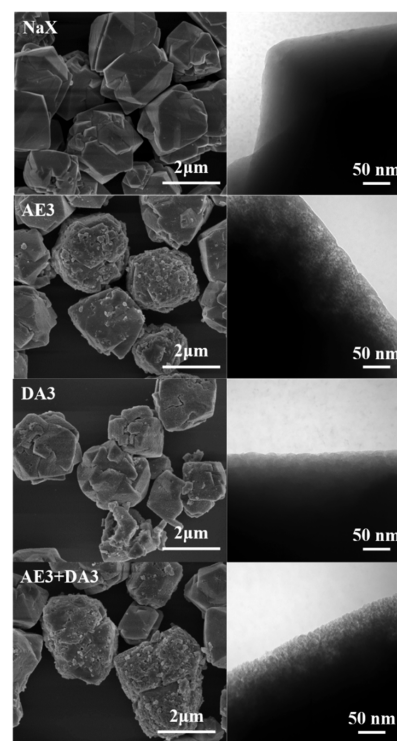

Figure 2. SEM and TEM images of the parent NaX zeolite and selected post-treated samples.

SEM and TEM images of other post-treated samples are provided in Figures S1 and S2, respectively. As seen, the parent NaX zeolite consists of polyhedron particles of 2−3 μm average size with smooth surfaces. The TEM image shows a smooth and uniform rim of the particles.

Table 1. Textural Properties of the Parent NaX and Selected Post-Treated Samples

| samples[a] | RC[b] (%) | SiO$_2$/Al$_2$O$_3$[c] | | | V_{total} (cm^3 g^{-1}) | V_{micro} (cm^3 g^{-1}) | V_{meso}[d] (cm^3 g^{-1}) |
		B	S	F			
NaX	100	2.5	2.8	2.4	0.34	0.26	0.08
AE1	82	2.4	–	–	0.31	0.25	0.06
AE3	24	2.4	2.2	2.9	0.31	0.05	0.26
AE5	9	2.4	–	–	0.31	0.00	0.31
DA1	72	2.6	–	–	0.34	0.25	0.09
DA3	64	2.7	12.3	2.5	0.38	0.24	0.14
AE1+DA1	65	2.8	–	–	0.34	0.23	0.11
AE1+DA3	49	3.3	–	–	0.30	0.23	0.07
AE3+DA1	37	3.2	–	–	0.40	0.14	0.26
AE3+DA3	29	3.5	9.6	3.0	0.43	0.09	0.34

[a]AE: ammonium-exchange; DA: dealumination; and AE+DA: the combination of ammonium-exchange and dealumination. [b]RC: relative crystallinities. [c]The SiO$_2$/Al$_2$O$_3$ of bulk phase (B), surface (S), and framework (F) were obtained by XRF, XPS, and ^{29}Si MAS NMR results, respectively. [d]$V_{meso} = V_{total} - V_{micro}$.
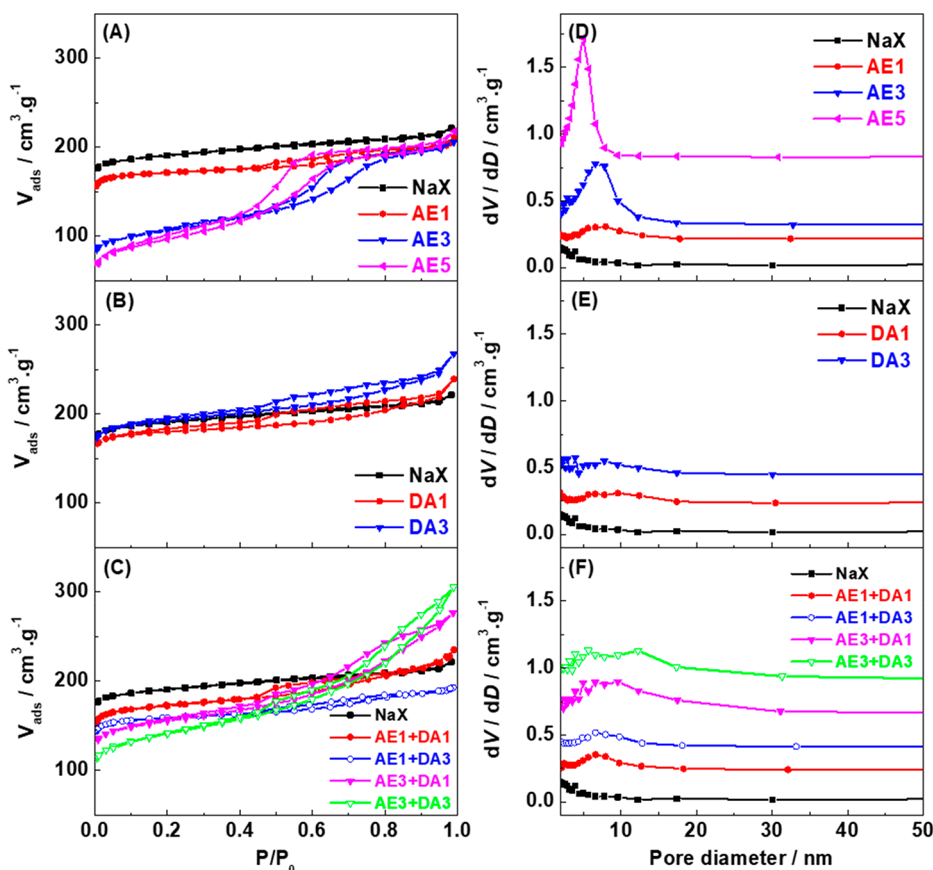
Figure 3. N_2 adsorption−desorption isotherms (A, B, and C) and mesopore size distribution curves (D, E, and F) of the parent NaX zeolite and selected post-treated samples, (A and D) AE samples, (B and E) DA samples, and (C and F) AE+DA samples.

It is also seen from the SEM images that all post-treated samples largely retain the polyhedron particles of the parent sample. However, for AE samples, the particle surfaces clearly become rough as shown in the SEM image of AE3. This roughness is found to increase with the increased intensity of AE treatment. The TEM image of the AE3 sample reveals partially collapsed rim of particles. This is consistent with the report that the framework structure of X zeolite becomes unstable when Na^+ is replaced by NH_4^+ and is being subjected to subsequent heat-treatment.[25]

Different from AE treatment, the particle morphology of DA samples appears to mainly duplicate that of the parent NaX. TEM analysis, however, reveals that the external particle surfaces also become uneven due to the dealumination effect.

For AE+DA samples, the particle morphology of the AE3+DA3 sample appears to be very similar to that of AE3. In addition, the TEM image reveals that the crystal structure is partially etched due to the combination treatment of AE and DA.

Figure 3 shows the N_2 adsorption−desorption isotherms and mesopore size distributions of the parent NaX zeolite and some selected post-treated samples. As shown in Figure 3A, the parent NaX zeolite exhibited a type-I isotherm according to IUPAC classification,[25] confirming it possesses a solely microporous structure.

For AE samples as seen in Figure 3A, with the increased AE treatment, the adsorption amount of nitrogen at very low relative pressures ($P/P_0 < 0.01$) decreases significantly, indicating a reduced microporosity in these samples. At the same time, the isotherms gradually convert from type-I to type-

IV, indicating the development of mesoporosity.[25,29] The hysteresis loop of the isotherms could be observed in the range of $P/P_0 = 0.4−0.8$. The mesopores are determined to be centered ∼5−7.5 nm with a relatively narrow size distributions as seen in Figure 3D.

For DA samples, Figure 3B shows that their isotherms remain similar to that of the parent NaX until $P/P_0 \sim 0.5$, where a mild hysteresis loop starts to develop. This indicates that a rather limited mesoporosity is introduced to these samples as the result of DA treatments. The small amount of mesopores in DA samples are also found to have sizes distributed between 5 and 15 nm as shown in Figure 3E.

Figure 3C shows that the mesoporosity of AE+DA samples could be mildly increased under intensified treatment conditions. Meanwhile, AE+DA samples still retain a certain degree of microporosity. The N_2 uptake of AE3+DA3 samples at very low relative pressures of $P/P_0 < 0.01$ remains higher than 100 cm^3 g^{-1}. These indicate that the combined AE+DA treatment is effective in introducing intracrystalline mesopores into X zeolites without severely destroying their microporosity. Furthermore, the treatment also allows the mesopore size distribution to be partially attuned as seen in Figure 3F. In contrast, such ability to control micro- or meso-porosities could not be achieved by solely relying on AE or DA treatment.

Table 1 and Table S1 summarize the textural properties of the parent NaX and post-treated samples obtained from their N_2 adsorption−desorption isotherms. It can be seen, the parent NaX has a high V_{micro} (0.26 cm^3 g^{-1}) due to its high
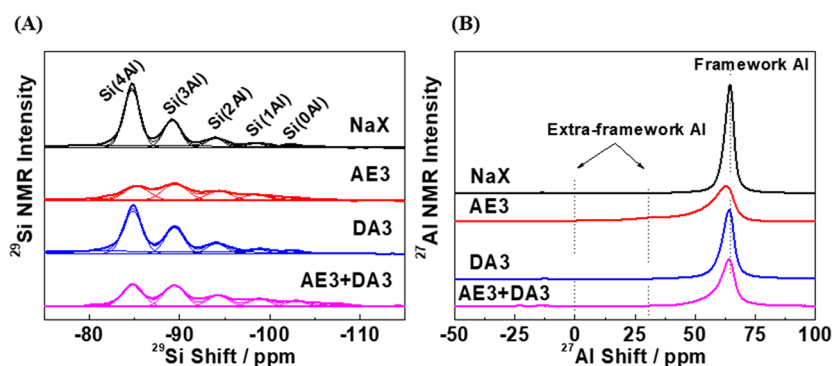
Figure 4. ^{29}Si (A) and ^{27}Al (B) MAS NMR spectra of the parent NaX and selected post-treated samples.

crystallinity and a very limited V_{meso} (0.08 cm^3 g^{-1}), mainly from the stacking between particles.

The AE treatment of parent NaX results in progressively increased V_{meso} and reduced V_{micro} with the increased treatment intensity. As seen in Table 1, AE1 exhibits slightly reduced V_{micro} (0.25 cm^3 g^{-1}) and V_{meso} (0.06 cm^3 g^{-1}) from NaX. However, the V_{micro} in AE3 decreases significantly to 0.05 cm^3 g^{-1}, while its V_{meso} increases many folds to 0.26 cm^3 g^{-1}. Although the V_{total} of AE3 (0.31 cm^3 g^{-1}) is close to that of NaX (0.33 cm^3 g^{-1}), most of the pore volume is contributed by the mesopores. For AE5, its microporosity is almost completely destroyed.

Unlike AE modification, the DA treatment does not cause significant loss to the microporosity of NaX. On the other hand, the mesoporosity of DA samples increases limitedly. For instance, the V_{micro} of DA3 is 0.24 cm^3 g^{-1}, which accounts for 96% of that of NaX. Meanwhile, the V_{meso} of DA3 increases by ~75% to 0.14 cm^3 g^{-1}.

The sequential AE+DA treatment delivers expected impact but in a more effective and controlled manner. For instance, the AE3+DA3 sample exhibits the highest V_{meso} (0.34 cm^3 g^{-1}) and, at the same time, retains a certain amount of V_{micro} (0.09 cm^3 g^{-1}). For comparison, when V_{meso} increases to 0.31 cm^3 g^{-1} as seen in AE5, its microporosity is completely destroyed. This means the AE+DA treatment could be an effective means to adjust and control textural properties of X zeolites. In this study, AE1+DA1, AE1+DA3, AE3+DA1, and AE3+DA3 are selected for catalytic evaluation, as they cover a broad range of micro- and meso-porosities.

3.1.2. Chemical Analysis of Post-Treated X Zeolites. Table 1 also lists SiO$_2$/Al$_2$O$_3$ ratios of the parent NaX and selected post-treated samples, including SiO$_2$/Al$_2$O$_3$ (B) for the bulk particles, SiO$_2$/Al$_2$O$_3$ (S) for the particle surfaces, and SiO$_2$/Al$_2$O$_3$ (F) for the zeolite framework. The SiO$_2$/Al$_2$O$_3$ (B) values are determined from XRF of the samples. The SiO$_2$/Al$_2$O$_3$ (S) are calculated by Si 2p and Al 2s XPS spectra presented in Figure S3. The SiO$_2$/Al$_2$O$_3$ (F) are calculated from ^{29}Si MAS NMR spectra according to the literature.[30] Figure 4 shows the ^{29}Si and ^{27}Al MAS NMR spectra of the NaX, AE3, DA3, and AE3+DA3 samples.

As seen in Table 1, the SiO$_2$/Al$_2$O$_3$ (B) of AE samples only decrease marginally from 2.5 of parent NaX to 2.4 and remains constant regardless of the AE treatment intensity. In contrast, the SiO$_2$/Al$_2$O$_3$ (B) of DA samples increases from 2.5 of parent NaX to 2.7 for DA3. Strikingly, the SiO$_2$/Al$_2$O$_3$ (B) of AE+DA samples increases significantly from 2.5 to 3.5 following intensified AE+DA treatments. The impact of post-treatments on SiO$_2$/Al$_2$O$_3$ (S) is much more significant. For

AE samples, the SiO$_2$/Al$_2$O$_3$ (S) decreases from 2.8 of parent NaX to 2.2 for AE3. For DA samples, the ratio increases drastically to 12.3 for DA3. This is consistent with the high SiO$_2$/Al$_2$O$_3$ (S) of 9.6 observed of the AE3+DA3 sample. As seen in Figure 4A, the ^{29}Si MAS NMR spectrum of parent NaX consists of five peaks at −86.5, −91.2, −95.9, −100.3, and −104.3 ppm, corresponding to Si(4Al), Si(3Al), Si(2Al), Si(1Al), and Si(0Al), respectively.[30] While similar NMR spectra are observed for the post-treated samples, the intensities of the characteristic peaks become weaker. The SiO$_2$/Al$_2$O$_3$ (F) of the samples are extracted from their NMR spectra and included in Table 1. As seen, SiO$_2$/Al$_2$O$_3$ (F) increases noticeably from 2.4 of parent NaX to 2.9 for AE3 but only increases slightly for DA3. However, for AE3+DA3, SiO$_2$/Al$_2$O$_3$ (F) increases significantly to 3.0. Generally, the impact of post-treatment on SiO$_2$/Al$_2$O$_3$ (F) is much milder than on SiO$_2$/Al$_2$O$_3$ (S), just like on the SiO$_2$/Al$_2$O$_3$ (B).

As seen from above, AE treatment is effective in increasing SiO$_2$/Al$_2$O$_3$ (F), DA treatment increases SiO$_2$/Al$_2$O$_3$ (S) strongly, and AE+DA treatment seems to exert most influence on increasing SiO$_2$/Al$_2$O$_3$ (B). This seems to suggest that the DA process mostly removes the framework Al species on the external surfaces of the zeolite crystals, likely by the hydrolysis of structural −O−Si−O−Al−O− through Na$_2$H$_2$EDTA.[23] This would result in framework Al species to form NaAl-(EDTA) complex cations with EDTA anions, resulting in the formation of mesopores as framework defect sites. The AE treatment, on the other hand, is capable of removing framework Al species throughout the zeolite crystals because the size of NH$_4^+$ is sufficiently small to enter into the interior of crystals.

Figure 4B shows the ^{27}Al MAS NMR spectra of parent NaX and selected post-treated X zeolites. It is seen that NaX exhibits a strong and narrow peak at 64.5 ppm which is attributed to tetrahedral Al sites, namely, framework Al species.[25] For the DA3 sample, the NMR peak remains similar to that of NaX in both peak position and width but with slightly decreased peak intensity. This indicates that the coordination environment of framework Al species in DA3 does not change, but the amount of framework Al species may have reduced slightly.

Different from DA3, the AE3 sample exhibits a noticeably broadened and asymmetrical ^{27}Al NMR peak and this peak also shifted to ca. 62.8 ppm. This indicates a change in the coordination environment of framework Al species in the AE3 sample. It was reported that the ^{27}Al NMR peaks of X zeolite at 0 and 31 ppm are associated with octahedral and pentahedral extra-framework Al species, respectively.[25,31] While no peak at
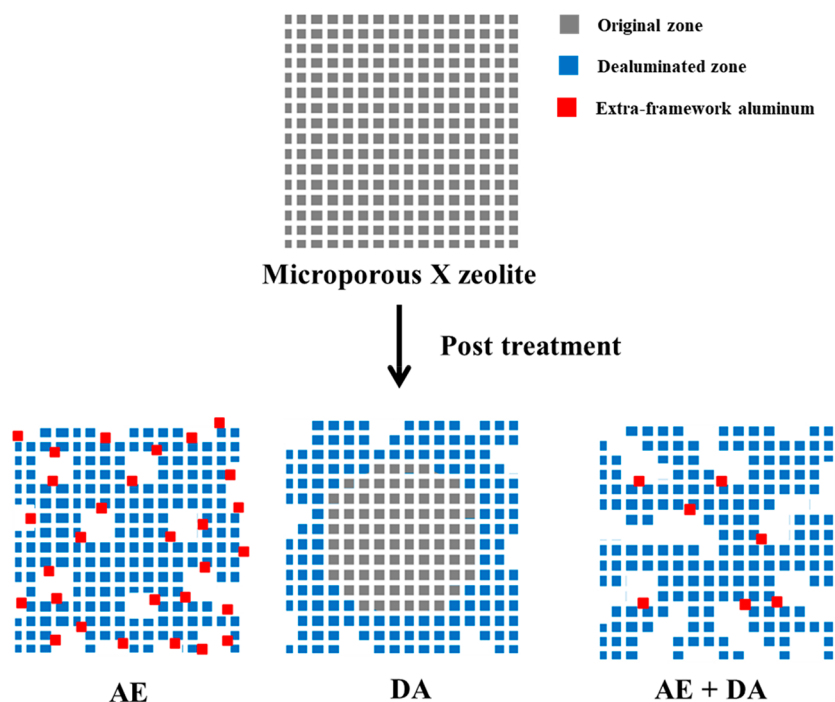
Figure 5. Schematic illustration of the pore structures of the parent NaX and different post-treated X zeolites.
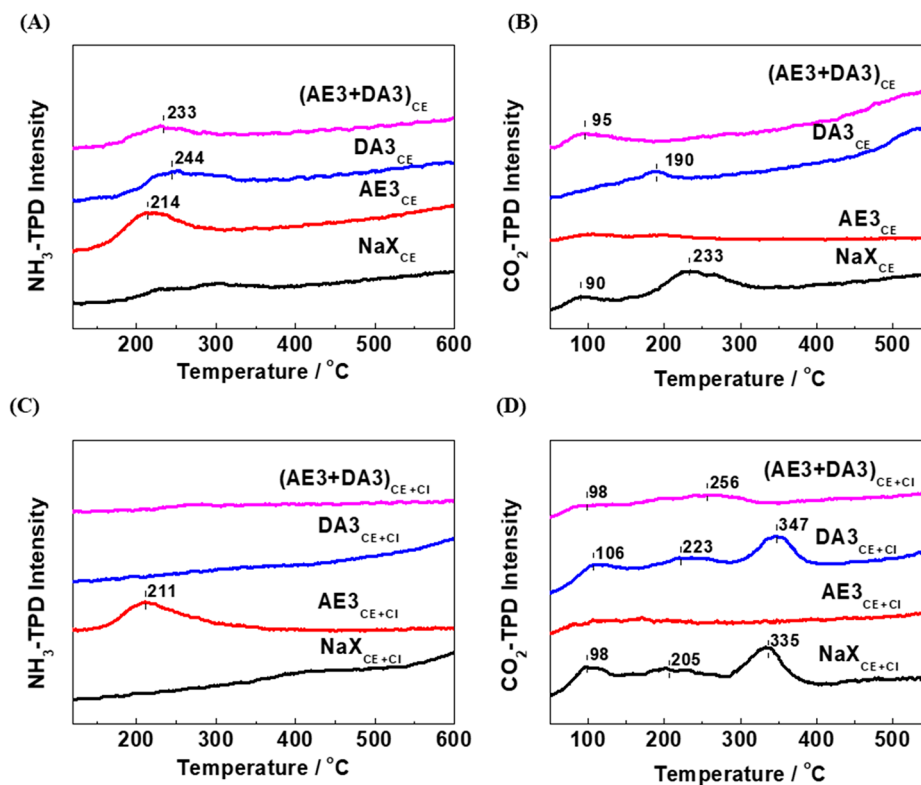

Figure 6. Analysis of acid−base properties of selected cesium modified mesoporous X zeolite catalysts, (A) NH_3-TPD curves of X_{CE} catalysts, (B) CO_2-TPD curves of X_{CE} catalysts, (C) NH_3-TPD curves of X_{CE+CI} catalysts, and (D) CO_2-TPD curves of X_{CE+CI} catalysts.

0 ppm for AE3 is observed, it is believed that there are pentahedral extra-framework Al species in AE3 which are responsible for asymmetrical shifting to lower ppm and broadening of its ^{27}Al NMR peaks. In this context, the decrease in SiO_2/Al_2O_3 (S) of the AE3 sample could be

attributed to the accumulation of extra-framework Al species on the particle surface.

The AE3+DA3 sample also exhibits a broadened ^{27}Al NMR peak at 64.5 ppm and the peak intensity falls in between that of DA3 and AE3. This result is consistent with the consideration that the extra-framework Al species produced by AE treatment

Table 2. Acidic Sites and Basic Sites Densities over Different Catalysts and their TOF Numbers for Side-Chain Alkylation of Toluene with Methanol

catalysts	acid/base densities[a] ($\mu mol\ g^{-1}$)				reaction rate[b] ($\times 10^{-3}\ \mu mol\ g^{-1}\ s^{-1}$)		TOF[c] ($\times 10^{-6}\ s^{-1}$)	
	acid	base	CsNaX	Cs_2O	ST	ST+EB	ST	ST+EB
NaX_{CE}	2.9	114.3	114.3	0	72	168	627	1473
$AE3_{CE}$	8.3	27.8	27.8	0	3	5	93	166
$DA3_{CE}$	5.9	33.0	33.0	0	48	89	1447	2690
$(AE3+DA3)_{CE}$	4.3	26.7	26.7	0	11	12	403	462
NaX_{CE+CI}	1.5	225.3	103.9	1439.2	11	182	101	1748
$AE3_{CE+CI}$	8.6	61.2	25.3	419.8	30	51	1167	2027
$DA3_{CE+CI}$	0.9	207.2	30.0	1979.0	5	195	166	6513
$(AE3+DA3)_{CE+CI}$	0.4	81.9	24.3	658.4	16	135	665	5560

[a]Acid/base densities are calculated from the amount of NH_3/CO_2 desorption over different catalysts. The base densities of CsNaX and Cs_2O are calculated based on the mass fractions of CsNaX and Cs_2O. [b]Reaction rate of toluene to "styrene" or "styrene + ethylbenzene". [c]Turn over frequencies of toluene to "styrene" or "styrene + ethylbenzene" over X_{CE} or X_{CE+CI} catalysts.

would be partially etched away by the subsequent DA treatment. This further supports that the AE+DA treatment is more effective in adjusting textural properties of X zeolites than the sole AE or DA treatment.

Figure S4 shows the FT-IR spectra of the NaX and selected post-treated samples. For NaX, the peaks located at 755 and 673 cm^{-1} are associated with framework symmetric stretching vibrations. The peaks at 560 and 462 cm^{-1} are related to tetrahedral vibrations of double six-membered rings (D6R) and O-T-O bending vibrations, respectively.[32] For AE samples, the intensities of these characteristic peaks weaken significantly with intensified AE treatment, as seen from the spectra of AE3 and AE5. Meanwhile, the corresponding peak intensities for DA1 and DA3 samples remain similar to those of the NaX. To be noted, the peak intensities for the AE+DA samples also decrease to varied extents. This again indicates that framework Al species in NaX zeolite is more vulnerable to the AE than the DA treatment, consistent with the SiO_2/Al_2O_3 results presented previously.

3.1.3. Location and Connectivity of Mesostructure in Post-Treated X Zeolites. Figure 5 depicts the location and connectivity of mesopores in AE, DA, and AE+DA samples based on the structure and SiO_2/Al_2O_3 analysis results presented in section 3.1.1 and 3.1.2. As seen, the parent NaX zeolite is mainly composed of uniform micropores. By AE treatment, some framework Al species are converted to extra-framework Al species, resulting in the formation of intra-crystalline mesopores. Moreover, these mesopores should distribute evenly over entire zeolite crystals because the extraction of framework Al species occur over the entire crystals. As to DA treatments, although some mesopores form over the external surface of the zeolite crystals by the partial removal external framework Al species, the interior of the crystals is not penetrated by this treatment. The combined AE+DA treatment could introduce mesopores into the zeolite crystals more effectively because the framework Al species could not only be extracted by the AE process but also be removed by the DA process. In addition, the mesopores in AE+DA samples are likely to be different from those of the AE or DA samples because the DA treatment could connect mesopores formed by the AE treatment through acid etching from the surface into the interior. Furthermore, the subsequent DA treatment also partially removes the extra-framework Al species formed in the AE step. This is beneficial in connecting the micropores and mesopores in the resulting samples.

3.2. Acidity and Basicity of X_{CE} or X_{CE+CI} Zeolites. In principle, toluene alkylation with methanol over acid catalysts produces virtually exclusively xylenes as styrene and ethylbenzene are formed by side-chain alkylation only over basic catalysts.[33] The acid−base properties of selected X_{CE} and X_{CE+CI} catalysts were evaluated by NH_3-TPD and CO_2-TPD measurements. Figure 6 shows the NH_3-TPD (A) and CO_2-TPD (B) curves of CE modified NaX, AE3, DA3, and AE3+DA3 zeolites, respectively. The results for the parent NaX, NaX_{CE}, and NaX_{CE+CI} are provided in Figure S5 as reference.

It can be seen that NaX_{CE} does not have an obvious ammonia desorption peak. This indicated that the acidity of NaX_{CE} is very weak. In addition, $DA3_{CE}$ and $(AE3+DA3)_{CE}$ catalysts exhibit weak ammonia desorption peaks at 244 and 233 °C, respectively. Compared with the above catalysts, $AE3_{CE}$ catalyst has obvious ammonia desorption peak at 214 °C, showing that the acidity of X zeolite is increased by the AE treatment. On the other hand, NaX_{CE} catalyst exhibits two CO_2 desorption peaks at 90 and 233 °C, respectively. The first peak is attributed to weakly adsorbed CO_2 desorption. The second peak is attributed to chemically adsorbed CO_2 desorption. Compared with NaX_{CE} catalyst, the peak areas of CO_2 desorption over $AE3_{CE}$, $DA3_{CE}$, and $(AE3+DA3)_{CE}$ catalysts reduce obviously. Table 2 presents the acidic site and basic site densities of various X_{CE} zeolites determined from the analysis of NH_3-TPD and CO_2-TPD results. It can be seen that the basic site densities of X_{CE} catalysts decrease over 70% by AE, DA, and AE+DA treatments.

Normally, the negative charges of X zeolite caused by framework Al species needs to be neutralized by Na$^+$. Basic sites are formed by ion-exchange of Na$^+$ with strong alkali metal cations, e.g., Cs$^+$. Thus, the extraction of framework Al species or dealumination inevitably causes the reduction of the basic sites amount over X_{CE} zeolite. Apparently, the basicities of the X_{CE} catalysts are strongly weakened by AE, DA, and AE+DA treatment.

Figure 6C,D exhibits the NH_3-TPD and the CO_2-TPD curves of CE+CI modified NaX, AE3, DA3, and AE3+DA3 catalysts, respectively. There is no ammonia desorption peak over NaX_{CE+CI}, $DA3_{CE+CI}$, and $(AE3+DA3)_{CE+CI}$ catalysts. It can be inferred that cesium impregnation neutralize the remaining weak acid sites over these catalysts. However, the $AE3_{CE+CI}$ catalyst still exhibits obvious ammonia desorption peak at 211 °C, indicating that there are still weak acid sites
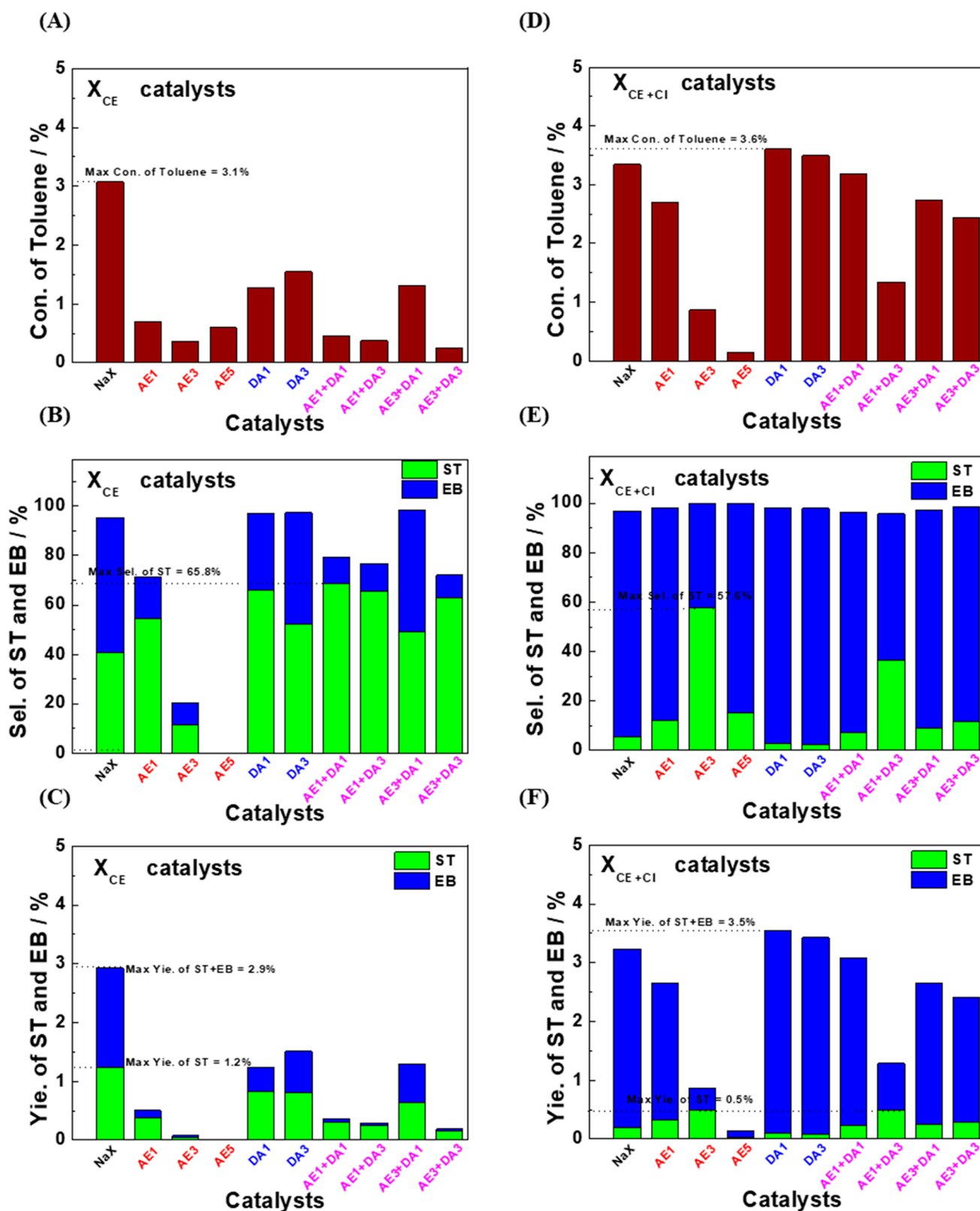
Figure 7. Catalytic performance for side-chain alkylation of toluene with methanol over different X zeolite catalysts, (A and D) the C_T over X_{CE} and X_{CE+CI} catalysts, respectively, (B and E) the S_{ST} and S_{EB} over X_{CE} and X_{CE+CI} catalysts, respectively, and (C and F) the Y_{ST} and Y_{EB} over X_{CE} and X_{CE+CI} catalysts, respectively (T = 698 K, p = 1 atm, WHSV = 2 h^{-1}, n_T/n_M = 6, $n_{N2}/n_{(T+M)}$ = 2).

existing over this catalyst. On the other hand, NaX$_{CE+CI}$ and DA3$_{CE+CI}$ catalyst exhibit new CO$_2$ desorption peaks at 335 and 347 °C, respectively. It can be inferred that the basicities of NaX$_{CE}$ and DA3$_{CE}$ catalysts is strengthened after cesium

impregnation. Meanwhile, we observed relatively weak CO$_2$ desorption peaks over AE3$_{CE+CI}$ and (AE3+DA3)$_{CE+CI}$ catalysts. Table 2 also presents the acidic site and basic site densities of various X$_{CE+CI}$ catalysts. It can be seen that the
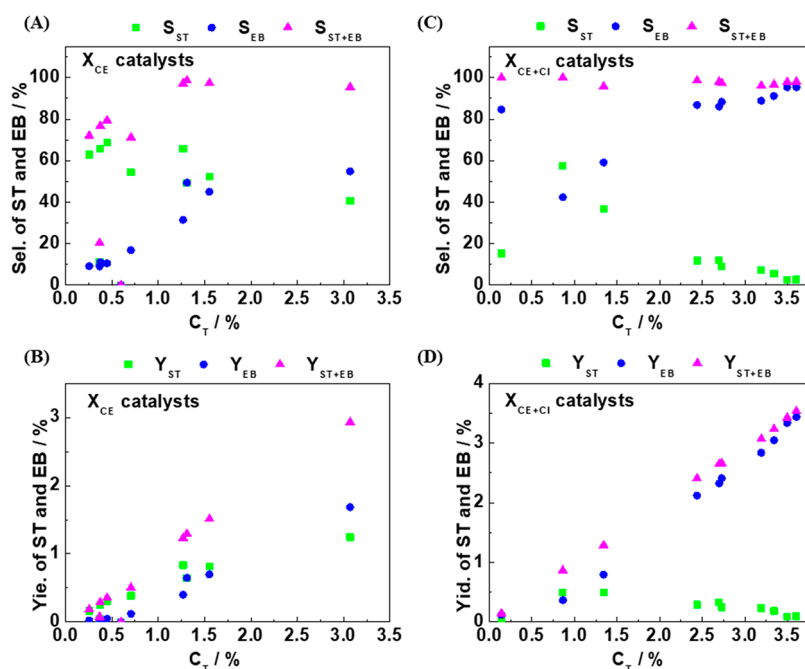
Figure 8. Relationship between the selectivity (or yields) of ST and EB and the conversion of toluene, (A and B) the scatter diagrams of S_{ST}, S_{EB}, and S_{ST+EB} over the X_{CE} (A) or X_{CE+CI} (B) catalysts vs the C_T, (C and D) the scatter diagrams of Y_{ST}, Y_{EB}, and Y_{ST+EB} over X_{CE} (C) or X_{CE+CI} (D) catalysts vs the C_T.

acidic site densities of X_{CE+CI} catalysts are generally lower than those of the X_{CE} catalysts except the AE3 sample. In addition, the basic sites densities of X_{CE+CI} catalysts are much higher than those of the X_{CE} catalysts due to the strong basicity of Cs_2O.

On the basis of the analysis of acid−base properties, we find that AE treatment increases the amount and strength of acid sites of X zeolites. The basicities of AE_{CE} and AE_{CE+CI} catalysts are always weaker than those of the NaX_{CE} and NaX_{CE+CI}. DA treatment partially removes external framework Al species, which results in the reduction in the amounts of ion-exchanged sites. Thus, the amounts of basic sites over DA_{CE} catalysts are less than those over NaX_{CE}. But we observe that the amounts of basic sites over DA_{CE} zeolites could be effectively increased by introducing Cs_2O species. Moreover, the effects of the AE +DA treatment on the acid−base properties of X zeolites are similar to the effects of the AE treatment although mild dealumination after ammonium-exchange could slightly reduce the amount of acid sites. Thus, the basicities of X_{CE} and X_{CE+CI} zeolites are weakened by both AE and AE+DA treatments.

The above discussion indicates that the acid−base property of basic X zeolite is related to the host framework SiO_2/Al_2O_3 ratio and the type and quantity of guest alkali metal cation species. The extraction of framework Al species during dealumination reduces the densities of basic sites in the X_{CE} zeolites. In contrast, introducing Cs_2O guest species increases the densities of these basic sites in the X_{CE} zeolites.

3.3. Catalytic Performance of Post-Treated X Zeolites. The catalytic performance of X_{CE} zeolites for side-chain alkylation of toluene with methanol was investigated. Figure 7 shows the conversion of toluene (C_T), selectivity (S), and yield (Y) of styrene (ST) and ethylbenzene (EB) over different X_{CE} zeolites. The corresponding gas phase products of the reactions are provided in Figure S6. The distribution of carbon species over different X_{CE} catalysts are also provided in Table S2.

As seen in Figure 7A, the C_T of the parent NaX_{CE} is 3.1%. Obviously, the C_T decreases more than 50% over X_{CE} regardless the detailed AE and/or DA treatments.

Figure 7B shows that S_{ST} and S_{ST+EB} of NaX_{CE} are 40.6% and 95.4%, respectively. It is immediately evident that S_{ST} increases for all X_{CE} zeolites except $AE3_{CE}$, while S_{EB} decreases for all X_{CE}. Noticeably, S_{ST+EB} of AE_{CE} decreases monotonously from 71.2% to ∼0 for $AE5_{CE}$. According to previous research,[18,19] the content of methanol and CO in the gas phase could reflect the catalytic activity of basic X zeolites. The higher content of CO in the gas phase, the higher catalytic activity of the catalyst. It is observed that the content of methanol increases and content of CO decreases in the gas phase over AE_{CE} catalysts as seen in Figure S6B. In contrast, the S_{ST+EB} remains higher than 95% over DA_{CE} catalysts, close to that of the NaX_{CE}. The methanol content increases and CO content decreases in the gas phase over DA_{CE} catalysts just as over AE_{CE} as seen in Figure S6D. The results over $(AE+DA)_{CE}$ zeolites seem to indicate the additive effects of AE+DA.

Figure 7C shows Y_{ST} and Y_{ST+EB} results for NaX_{CE} and X_{CE}. Clearly, both yields are lower for post-treated X_{CE} than NaX_{CE} mostly resulting from the decreased C_T.

Parallelly, the catalytic performance of NaX_{CE+CI} and post-treated X_{CE+CI} zeolites for the side-chain alkylation of toluene with methanol were also investigated, and the results are also included in Figure 7. Similarly, the gas phase product and carbon species distributions for the reactions over these zeolites are also provided in Figure S7 and Table S3, respectively.

As shown in Figure 7D, the C_T only increases slightly from 3.1% for NaX_{CE} to 3.3% for NaX_{CE+CI}. However, the corresponding S_{ST} decreases significantly from 54.4% over NaX_{CE} to 5.6% over NaX_{CE+CI}. In addition, Figure S7D indicates that the content of CO in the gas phase increased dramatically over the NaX_{CE+CI} catalyst. The changes of C_T,

S_{ST}, and the content of CO in the gas phase product over NaX_{CE} and NaX_{CE+CI} are consistent with previous results.[19]

Among the X_{CE+CI} zeolite catalysts, the S_{ST+EB} are around 96−100%, indicating that most of the alkylation products are ST or EB (Figure 7E). To be noted, the S_{ST} of most catalysts are lower than 20% which also means that introducing Cs_2O into X_{CE} zeolites is beneficial to the formation of EB.

For AE_{CE+CI} catalysts, the C_T decreases monotonously with the intensifying of AE modification (Figure 7D) indicating that AE treatment decreases the catalytic activity. This could be further proved by the amount of CO in gas phase decreases dramatically over $AE3_{CE+CI}$ and $AE5_{CE+CI}$ samples (Figure S7B). For DA_{CE+CI} catalysts, the C_T increase slightly (Figure 7D). Meanwhile, the amount of CO over DA_{CE+CI} catalysts increases to 74−76% (Figure S4D). These results indicate that DA treatment is beneficial to improve the catalytic activity of X_{CE+CI} zeolites. Concerning to $(AE+DA)_{CE+CI}$ catalysts, the C_T decreases to different extents (Figure 7D). However, the C_T of $(AE1+DA1)_{CE+CI}$ is higher than that of $AE1_{CE+CI}$ catalysts. Same phenomena are also observed over $(AE3+DA1)_{CE+CI}$ and $AE3_{CE+CI}$ catalysts. These phenomena indicate that mild dealumination after ammonium-exchange is beneficial to improve the catalytic activity of X_{CE+CI} zeolites.

Although S_{ST+EB} over X_{CE+CI} zeolites are around 96−100%, it is found that the S_{ST} decreases obviously. Thus, the Y_{ST} over the X_{CE+CI} catalysts is lower than 0.5% and the Y_{ST+EB} is close to C_T (Figure 7F).

Figure 8 shows the scatter diagram of the selectivity and yield of ST, EB, and ST+EB over X_{CE} or X_{CE+CI} zeolites versus the C_T, respectively. For X_{CE} zeolites, Figure 8A shows that the S_{EB} basically increases with the increasing of C_T. Figure 8B indicates that both Y_{ST} and Y_{EB} increase with the increasing C_T. But the Y_{EB} increases faster than Y_{ST} when the C_T increases to 3.0%. This phenomenon is even more obvious over X_{CE+CI} zeolite catalysts (Figure 8C). In addition, the changes of S_{ST} and S_{EB} exhibit opposite trends with the increasing C_T. This indicates that high catalytic activity and high S_{ST} are not compatible over basic X zeolite catalysts. Moreover, Figure 8D indicates that the Y_{EB} increases monotonously while the Y_{ST} first increases and then decreases.

The above comparison of the catalytic performance is established on the overall catalytic activity. However, the overall catalytic activity, e.g., the C_T, is not able to reflect the catalytic activity of individual active site. Thus, to understand the catalytic activity of individual active site, the TOF numbers are calculated. The TOF numbers over selected X_{CE} and X_{CE+CI} catalysts are presented in Table 2 and plotted in Figure 9 for comparison. It can be seen that the TOF_{ST+EB} number over $DA3_{CE}$ is higher than that of NaX_{CE}. In contrast, the TOF_{ST+EB} numbers over $AE3_{CE}$ and $(AE3+DA3)_{CE}$ are obvious lower than that of NaX_{CE}. On the other hand, the TOF_{ST+EB} over NaX_{CE+CI} is slightly higher than that of NaX_{CE} and it is almost contributed by TOF_{EB}. Surprisingly, the TOF_{ST+EB} numbers over X_{CE+CI} catalysts increased significantly by DA or AE+DA treatments. But TOF_{EB} also mainly contributes them.

3.4. Discussion. *3.4.1. Yield and Pore Structure in X Zeolites.* The scatter diagrams of total yield of styrene and ethylbenzene (Y_{ST+EB}) of different X zeolite catalysts versus their original micropore (V_{micro}) and mesopore (V_{meso}) volumes before modification are plotted in Figure 10. This enables one to understand the effects of the changes of
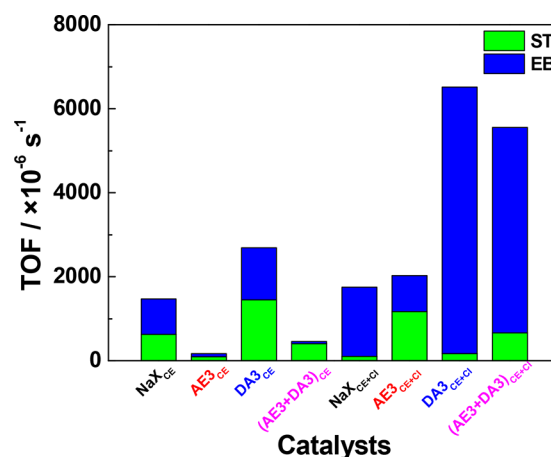

Figure 9. Influence of different post-treatments to the turn over frequencies (TOF) of side-chain alkylation of toluene with methanol over X_{CE} and X_{CE+CI} catalysts.

intrinsic pore structure on the catalytic performance of X_{CE} and X_{CE+CI} catalysts.

For X_{CE} zeolites, as seen in Figure 10A, there is no obvious dependence of Y_{ST+EB} on V_{micro}. While a number of the zeolites have similar levels of V_{micro} to that of NaX, their Y_{ST+EB} are significantly lower than NaX. Additionally, those zeolites with $V_{micro} < 0.05$ cm^3 g^{-1} present very low Y_{ST+EB} (<0.5%). It is also evident from Figure 10B that increasing V_{meso} does not seem beneficial to improve Y_{ST+EB} over X_{CE} zeolites.

For X_{CE+CI} zeolites, as seen in Figure 10C,D, Y_{ST+EB} is dominantly dictated by the V_{micro} than V_{meso}. Higher V_{micro} clearly promotes higher Y_{ST+EB} and the same could not be said for V_{meso}. This is demonstrated by comparing the Y_{ST+EB} over AE3 and DA 1, for example.

These results seem to indicate that while high micropore volume may not necessarily bring high catalytic activity for the X zeolites, an appropriate micropore volume seems to be indispensable to support the side-chain alkylation of toluene with methanol. Additionally, mesopores do not seem to play a decisive role in the catalytic performance of these zeolites.

3.4.2. Yield and Acidity-Basicity of X Zeolites. Figure 11 presents the floating bar charts of basic and acidic sites densities versus the yield of styrene (Y_{ST}), ethylbenzene (Y_{EB}), and styrene + ethylbenzene (Y_{ST+EB}) over X_{CE} and X_{CE+CI} zeolites.

Figure 11A indicates that too high or too low basic sites densities result in very low Y_{ST}. For example, the basic site densities of NaX_{CE+CI} and $DA3_{CE+CI}$ catalysts are more than 200 μmol g^{-1} and their Y_{ST} is lower than 0.2%. On the contrary, the basic site densities of $AE3_{CE}$ and $(AE3+DA3)_{CE}$ are less than 12 μmol g^{-1} and their Y_{ST} is also extremely low. To be noted, the highest Y_{ST} is obtained over the NaX_{CE} catalyst and its basic and acidic site densities are in the middle position among the investigated catalysts.

Figure 11B indicates that the Y_{EB} basically increases with the increase of basic site densities. Meanwhile, it decreases with the increasing of acidic site densities. This could be easily seen from the results of $DA3_{CE+CI}$, NaX_{CE}, and $AE3_{CE}$. Figure 11C shows that the relationship between the Y_{ST+EB} and the basic or acidic sites densities is very similar to that of Y_{EB}, which means that higher basic sites densities resulted in higher Y_{ST+EB}.

The above results proved that the acid−base properties of X zeolites strongly influence the yield of ST and EB. As the
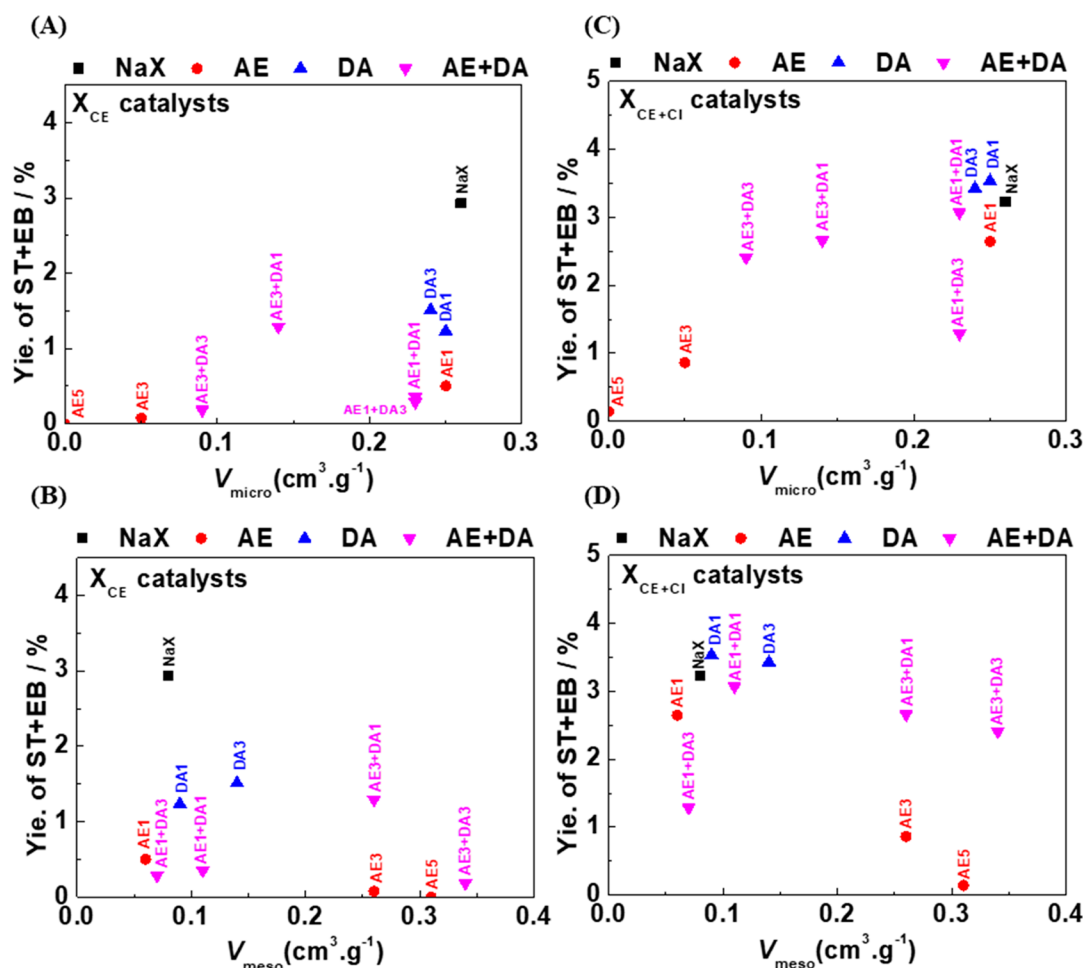
Figure 10. Relationship between Y_{ST+EB} of different X zeolite catalysts and their original micropore (V_{micro}) and mesopore (V_{meso}) volumes before modification. (A) Y_{ST+EB} vs V_{micro} over X_{CE} catalysts, (B) Y_{ST+EB} vs V_{meso} over X_{CE} catalysts, (C) Y_{ST+EB} vs V_{micro} over X_{CE+CI} catalysts, and (D) Y_{ST+EB} vs V_{meso} over X_{CE+CI} catalysts.

previous literature indicated,[34,35] side-chain alkylation of toluene with methanol to ST needs enough strong basicity. However, if the basicity is too strong, the side-chain alkylation product will be gradually changed from ST to EB. Thus, balanced basicity is necessary to maximize the yield of ST. Keeping increasing the basicity of X zeolites results in the fast increase of the yield of EB.

3.4.3. TOF of Toluene to ST and EB over X Zeolites. Figure 12 plots the TOF_{ST+EB} numbers presented in Table 2 against intrinsic V_{meso} of X_{CE} and X_{CE+CI} zeolites. For X_{CE} catalysts, although intrinsic V_{meso} of $AE3_{CE}$ and $(AE3+DA3)_{CE}$ increase significantly, the TOF_{ST+EB} number reduces obviously. Surprisingly, although the V_{meso} of $DA3_{CE}$ increases marginally, the TOF_{ST+EB} number is clearly higher than that of NaX_{CE}. For X_{CE+CI} catalysts, it is evident that CE+CI modification has the dominant effect on TOF_{ST+EB} numbers. Although $DA3_{CE+CI}$ has only modest V_{meso}, it displays the highest TOF_{ST+EB} number. Obviously, the TOF_{ST+EB} numbers could be dramatically increased by introducing appropriate mesopores through effective post-treatments, e.g., DA treatment. These results indicate that although the amounts of active centers are reduced by DA or AE+DA post-treatments, the presence of intracrystalline mesopores enhance the diffusion of molecules and improved the accessibilities of the retained active sites, which results in obviously increased Cs^+X^- site activity for side-chain alkylation of toluene with methanol.

As pointed out by Sidorenko et al.[8] and Yashima et al.,[9] ST is produced by the side-chain alkylation of toluene with formaldehyde formed by dehydrogenation of methanol and a part of this ST is further hydrogenated to EB. In addition, Itoh et al.[13] indicated that specific configurations of basic and acidic sites with steric restrictions are required for the side-chain alkylation of toluene. Such configurations could only be achieved by strong alkali metal cations, such as Cs^+, ion-exchanged FAU zeolites. Wieland et al.[10] and Palomares et al.[12] also indicated that the supercages of basic FAU zeolites are indispensable for the transition state formation.

It is clear that the catalytic performance of X zeolites for side-chain alkylation of toluene with methanol not only depends on their pore structures but also relies on their acid–base properties. On the one hand, the micropore structures of X zeolites determine the activation of reactants and formation of transition states while the mesopore structures enhance the diffusion process of molecules and the accessibilities of active sites. On the other hand, the changes of zeolite acid–base properties seem to have much stronger influence to the catalytic activity and selectivity.

In this research, post-treatment not only changes the pore structure but also changes the acid–base properties. The increase in V_{meso} is at the expense of V_{micro}; it could be inferred that the amounts of active sites of X zeolites decrease because of the post-treatments. Although the introduced mesoporosity
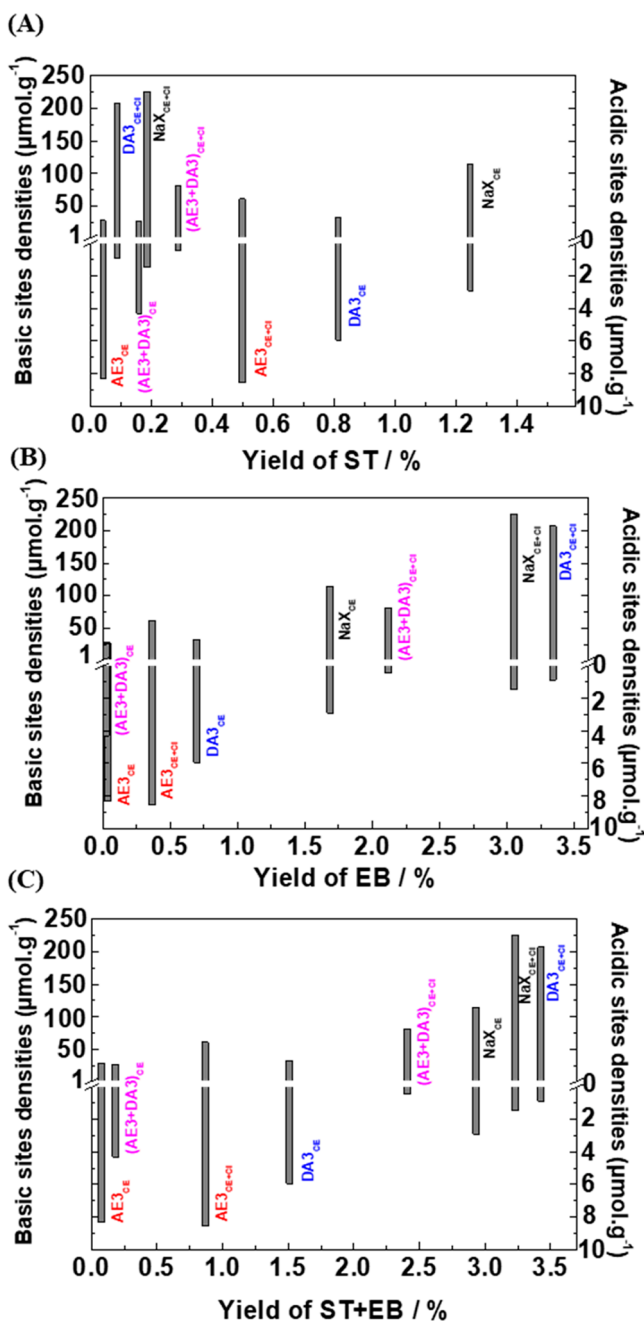
Figure 11. Floating bar charts of the basic and acidic sites densities vs the yield of styrene (Y_{ST}), ethylbenzene (Y_{EB}), and styrene + ethylbenzene (Y_{ST+EB}) over different X_{CE} or X_{CE+CI} catalysts. (A) The basic and acidic site densities vs the Y_{ST}, (B) the basic and acidic site densities vs the Y_{EB}, and (C) the basic and acidic sites densities vs the Y_{ST+EB}.

Figure 12. Effects of intrinsic mesopore volumes of X zeolites on the TOF of toluene to styrene and ethylbenzene over the basic X zeolites.

intensifies the mass transfer of reactants and products, diffusion limitation may not be the principal factors to limit the catalytic performance. The basic sites densities are proven to have more important influences to the catalytic performance. Consequently, high V_{micro} is useful to obtain good catalytic activity. But it could not necessarily bring high yield of ST and EB. However, if the V_{micro} decreases to a very low level, the catalytic activity would be ruined.

Increasing the V_{meso} of X zeolite by AE, DA, and AE+DA treatments resulted in the losses of framework Al species, which reduces the basic site densities and further decreases the
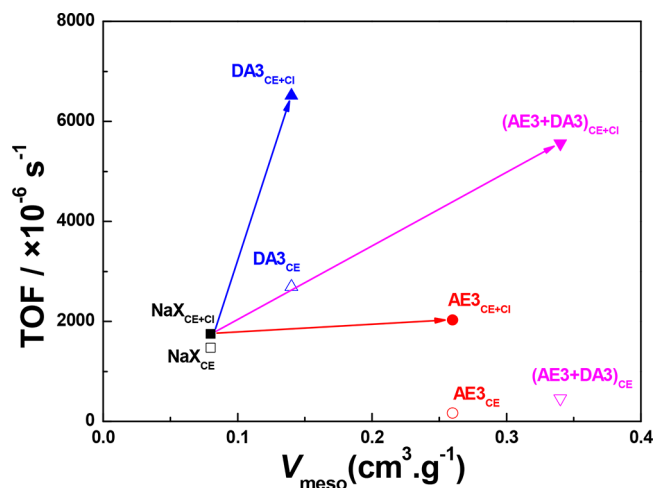
catalytic activity of X_{CE} catalysts for side-chain alkylation of toluene with methanol. But if the mesoporous X zeolite could be modified by CE+CI, the negative effects brought by reduction of basic site densities could be recovered by introducing Cs_2O. Thus, $DA3_{CE+CI}$ catalyst demonstrates slightly higher overall catalytic activity than that of NaX_{CE+CI} zeolite as well as the highest Cs^+X^- site activity for side-chain alkylation of toluene with methanol because it has the advantages of both high micropore volume for catalyzing reaction and appropriate mesopore volume to strengthen diffusion. More importantly, strong alkali metal modification of CE+CI provides enough amounts of basic sites. But NaX_{CE} zeolite possesses the highest Y_{ST}, proving that there should be balanced basicity to produce ST by side-chain alkylation of toluene with methanol. It means that too high or too low density of basic sites is not beneficial to pursue high Y_{ST}.

Consequently, the results of this work supported the catalytic mechanism proposed by Itoh et al.[13] and Weiland et al.[10] It was indicated that methanol first converted to formaldehyde over a single Cs^+X^- basic site, and toluene is strongly retained on the Lewis acid site (Cs^+) via delocalized π-electrons of aromatic ring interacting with the empty electron orbitals of Cs^+. Formaldehyde formed attacks the methyl group of toluene to produce phenyl ethanol. The negatively polarized benzyl carbon ($C^{\delta-}$) and the positively polarized carbonyl carbon ($C^{\delta+}$) form a new C−C bond. Then, the phenyl ethanol dehydrates to styrene. This catalytic mechanism demands at least two Cs^+X^- sites with specific configurations to support the side-chain alkylation of toluene with formaldehyde needs.

In this work, the framework Al species are extracted or etched by the AE and/or DA post treatments, and this reduces the amount of available ion-exchange sites. This is responsible for the observed reduction in overall activity of the X_{CE} zeolites due to the reduced quantity of effective dual Cs^+X^- sites. This reduction in overall activity could be compensated by Cs_2O impregnation of X_{CE} zeolites according to our previous work.[18,19] Meanwhile, the increased site-activity observed by introducing mesopores indicates that the accessibility to the dual Cs^+X^- active centers has been enhanced.

This systematic work provides the following insights on the designing consideration of effective X zeolite catalysts for side-chain alkylation of toluene with methanol.

First and foremost, the intrinsic micropore structure of X zeolite plays critical roles in the activation of reactants and promoting transition state formation for side-chain alkylation of toluene with methanol. Although mesopores do not seem to play a decisive role in the catalytic performance, introducing appropriate amounts of mesopores into microporous X zeolites by post-treatments could enhance the diffusions of reactants and products and improve the accessibility of retained active sites. In addition, the overall catalytic activity for side-chain alkylation of toluene over X zeolites increases with the increasing density of basic sites. The framework Al species should be protected in the process of introducing mesopores to retain high aluminum content in the zeolite framework.

The basicities of the zeolites could be strengthened by CE and CE+CI modification. But there should be balanced basic site and acid site densities to maximize the yield of ST by side-chain alkylation of toluene with methanol. That is why boric acid[1,35] has always been used to modify the acid—base properties of CsNaX catalysts to improve the yield of ST.

With all learned in this work, the hierarchical faujasite nanosheets[36,37] and nanosized faujasite particles[38,39] synthesized by *in situ* methods may provide new opportunities for side-chain alkylation of toluene with methanol because the micropore structure of X zeolite was well reserved by increasing the mesopore volumes for these materials. In addition, the content of framework Al species could be well adjusted. Probably, these kinds of X zeolites could effectively improve the accessibility of active centers in micropores and enhance the diffusion of molecules without reducing the amounts of active sites.

4. CONCLUSIONS

This work sets out to investigate the effects of post chemical treatments to the pore structure and acid—base property of the NaX zeolite with the aim to produce high performance catalysts for side-chain alkylation of toluene with methanol. Overall, this study reveals that X zeolites with a high micropore volume, appropriate mesopore volume, and abundant framework Al species are the most effective for the side-chain alkylation of toluene with methanol. Furthermore, it is the basicity of the X zeolites rather than their pore structure that dictates the catalytic activity and selectivity for this alkylation reaction. The detailed findings of this study are summarized below. (1) Mesopores can be introduced into microporous NaX via AE treatment by converting framework Al species to extra-framework Al species or via DA treatment by etching framework Al species but at the expenses of micropores. The combined AE+DA treatment is found to be most effective in controlling and adjusting the formation of mesopores and, at the same time, retaining some amount of micropores. (2) While the presence of mesopores generally enhances the molecular diffusion conditions, the restriction effect of micropores is found to be most critical for the side-chain alkylation reaction. (3) Inevitably, the post chemical AE and/ or DA treatments reduce the basicity of the resulting X_{CE} zeolites due to the removal of framework Al species. However, this reduction in basicity is compensated by the subsequent cesium impregnation. Essentially, the catalytic activity for the side-chain alkylation reaction increases with increased density of basic sites in the X zeolites. (4) The parent NaX_{CE} catalyst delivers the highest Y_{ST} due to its high V_{micro} and balanced basicity. Among different post-treated X_{CE} or X_{CE+CI} catalysts, DA_{CE+CI} catalyst possesses the highest Y_{ST+EB} as well as the

highest TOF_{ST+EB}. Although post-treatments decrease the amounts of basic sites over X_{CE} zeolites, the site activity of X_{CE} zeolites could be improved by introducing appropriate amount of mesopores and/or Cs_2O.

■ ASSOCIATED CONTENT

ⓢ Supporting Information

The Supporting Information is available free of charge at https://pubs.acs.org/doi/10.1021/acs.iecr.1c02179.

Additional characterization data and reaction results, including (1) SEM images of parent NaX zeolite and different post-treatment samples, (2) TEM images of parent NaX zeolite and different post-treatment samples, (3) XPS and FT-IR spectra of parent NaX and selected mesoporous X zeolite, (4) analysis of acid—base property and pore structures of NaX and its cesium modified catalysts, (5) comparison of catalytic performance and gas phase product distribution over different X_{CE} and X_{CE+CI} zeolite catalysts, (5) textural properties of parent NaX zeolite and different post-treated X zeolite samples, (6) carbon species distribution and catalytic performance of side-chain alkylation of toluene with methanol over selected X_{CE} and X_{CE+CI} catalysts, and (7) elemental analyses and pore structure properties of parent NaX and its cesium modified catalysts (PDF)

■ AUTHOR INFORMATION

Corresponding Authors

Min Liu — *State Key Laboratory of Fine Chemicals, PSU-DUT Joint Center for Energy Research, School of Chemical Engineering, Dalian University of Technology, Dalian, Liaoning Province 116024, P.R. China;* ⓞ orcid.org/0000-0003-2291-6266; Email: lium@dlut.edu.cn

Hong Yang — *Department of Mechanical Engineering, The University of Western Australia, Perth, WA 6009, Australia;* Email: hong.yang@uwa.edu.au

Xinwen Guo — *State Key Laboratory of Fine Chemicals, PSU-DUT Joint Center for Energy Research, School of Chemical Engineering, Dalian University of Technology, Dalian, Liaoning Province 116024, P.R. China;* ⓞ orcid.org/0000-0002-6597-4979; Email: guoxw@dlut.edu.cn

Authors

He Han — *State Key Laboratory of Fine Chemicals, PSU-DUT Joint Center for Energy Research, School of Chemical Engineering, Dalian University of Technology, Dalian, Liaoning Province 116024, P.R. China;* ⓞ orcid.org/0000-0001-6012-4126

Chuan Shi — *State Key Laboratory of Fine Chemicals, PSU-DUT Joint Center for Energy Research, School of Chemical Engineering, Dalian University of Technology, Dalian, Liaoning Province 116024, P.R. China;* ⓞ orcid.org/0000-0002-5152-7561

Shutao Xu — *Dalian Institute of Chemical Physics, Chinese Academy of Science, Dalian, Liaoning Province 116023, P.R. China;* ⓞ orcid.org/0000-0003-4722-8371

Yingxu Wei — *Dalian Institute of Chemical Physics, Chinese Academy of Science, Dalian, Liaoning Province 116023, P.R. China*

Zhongmin Liu — *Dalian Institute of Chemical Physics, Chinese Academy of Science, Dalian, Liaoning Province 116023, P.R. China;* ⓞ orcid.org/0000-0002-7999-2940

Chunshan Song − *State Key Laboratory of Fine Chemicals, PSU-DUT Joint Center for Energy Research, School of Chemical Engineering, Dalian University of Technology, Dalian, Liaoning Province 116024, P.R. China; Department of Chemistry, Faculty of Science, The Chinese University of Hong Kong, Shatin, NT, Hong Kong 999077, P.R. China;* ⓞ orcid.org/0000-0003-2344-9911

Complete contact information is available at:
https://pubs.acs.org/10.1021/acs.iecr.1c02179

Notes
The authors declare no competing financial interest.

REFERENCES

(1) Hong, Z.; Xiong, C.; Zhao, G.; Zhu, Z. Side-chain alkylation of toluene with methanol to produce styrene: an overview. *Catal. Sci. Technol.* **2019**, *9*, 6828−6840.

(2) Perego, C.; Ingallina, P. Recent advances in the industrial alkylation of aromatics: new catalysts and new processes. *Catal. Today* **2002**, *73*, 3−22.

(3) Atanda, L. A.; Aitani, A. M.; Al-Khattaf, S. S. Experimental and kinetic studies of ethyltoluenes production via different alkylation reactions. *Chem. Eng. Res. & Des.* **2015**, *95*, 34−46.

(4) Cejka, J.; Silková, N.; Wichterlová, B.; Eder-Mirth, G.; Lercher, J. A. Decisive role of transport rate of products for zeolite para-selectivity: Effect of coke deposition and external surface silylation on activity and selectivity of HZSM-5 in alkylation of toluene. *Zeolites* **1996**, *17*, 265−271.

(5) Li, X.; Lu, J.; Li, Y.; Yu, J. Roles of Hydroxyl Groups During Side-Chain Alkylation of Toluene with Methanol over Zeolite Na-Y: A Density Functional Theory Study. *Chin. J. Chem.* **2017**, *35*, 716−722.

(6) Martín, A. J.; Mitchell, S.; Scholder, O.; Verel, R.; Hauert, R.; Bernard, L.; Jensen, C.; Schwefer, M.; Pérez-Ramírez, J. Elucidating the Distribution and Speciation of Boron and Cesium in BCsX Zeolite Catalysts for Styrene Production. *ChemPhysChem* **2018**, *19*, 437−445.

(7) Wang, H.; Wang, B.; Wen, Y.; Huang, W. High-Yielded Side-Chain Alkylation from Toluene and Methanol Over K3PO4/CsX. *Catal. Lett.* **2017**, *147*, 161−166.

(8) Sidorenko, Y. N.; Galich, P. N.; Gutirya, V. S. Condensation of toluene and methanol upon synthetic zeolites containing ion-exchange cations of alkali metals. *Dokl. Akad. Nauk. SSSR* **1967**, *173*, 132−133.

(9) Yashima, T.; Sato, K.; Hayasaka, T.; Hara, N. Alkylation on synthetic zeolites: III. Alkylation of toluene with methanol and formaldehyde on alkali cation exchanged zeolites. *J. Catal.* **1972**, *26*, 303−312.

(10) Wieland, W. S.; Davis, R. J.; Garces, J. M. Side-Chain Alkylation of Toluene with Methanol over Alkali-Exchanged Zeolites X, Y, L, and β. *J. Catal.* **1998**, *173*, 490−500.

(11) Hattori, H.; Amusa, A. A.; Jermy, R. B.; Aitani, A. M.; Al-Khattaf, S. S. Zinc oxide as efficient additive to cesium ion-exchanged zeolite X catalyst for side-chain alkylation of toluene with methanol. *J. Mol. Catal. A: Chem.* **2016**, *424*, 98−105.

(12) Palomares, A. E.; Eder-Mirth, G.; Rep, M.; Lercher, J. A. Alkylation of Toluene over Basic Catalysts—Key Requirements for Side Chain Alkylation. *J. Catal.* **1998**, *180*, 56−65.

(13) Itoh, H.; Miyamoto, A.; Murakami, Y. Mechanism of the side-chain alkylation of toluene with methanol. *J. Catal.* **1980**, *64*, 284−294.

(14) Philippou, A.; Anderson, M. W. Solid-state NMR investigation of the alkylation of toluene with methanol over basic zeolite X. *J. Am. Chem. Soc.* **1994**, *116*, 5774−5783.

(15) Xiangsheng, W.; Guiru, W.; Dongmin, S.; Chengbi, F.; Ming, W. Side-chain alkylation of toluene with methanol on KX/KZSM-5 binary zeolite catalysts. *Zeolites* **1991**, *11*, 254−257.

(16) Alabi, W. O.; Tope, B. B.; Jermy, R. B.; Aitani, A. M.; Hattori, H.; Al-Khattaf, S. S. Modification of Cs-X for styrene production by side-chain alkylation of toluene with methanol. *Catal. Today* **2014**, *226*, 117−123.

(17) Jiang, J.; Lu, G.; Miao, C.; Wu, X.; Wu, W.; Sun, Q. Catalytic performance of X molecular sieve modified by alkali metal ions for the side-chain alkylation of toluene with methanol. *Microporous Mesoporous Mater.* **2013**, *167*, 213−220.

(18) Han, H.; Liu, M.; Ding, F.; Wang, Y.; Guo, X.; Song, C. Effects of Cesium Ions and Cesium Oxide in Side-Chain Alkylation of Toluene with Methanol over Cesium-Modified Zeolite X. *Ind. Eng. Chem. Res.* **2016**, *55*, 1849−1858.

(19) Han, H.; Liu, M.; Nie, X.; Ding, F.; Wang, Y.; Li, J.; Guo, X.; Song, C. The promoting effects of alkali metal oxide in side-chain alkylation of toluene with methanol over basic zeolite X. *Microporous Mesoporous Mater.* **2016**, *234*, 61−72.

(20) Yu, Q.; Li, J.; Wei, C.; Zeng, S.; Xu, S.; Liu, Z. Role of ball milling during Cs/X catalyst preparation and effects on catalytic performance in side-chain alkylation of toluene with methanol. *Chin. J. Catal.* **2020**, *41*, 1268−1278.

(21) Han, Q.; Li, P.; Zhang, Y.; Lu, P.; Xu, L.; Guo, H.; Xu, L. Conversion of MeOH and Toluene into Styrene and Ethylbenzene Using Composite Catalysts Containing MeOH Dehydrogenation Components. *ChemCatChem* **2019**, *11*, 1610−1614.

(22) Xie, J.; Kaliaguine, S. Zeolite ball milling as a means of enhancing the selectivity for base catalyzed reactions. *Appl. Catal., A* **1997**, *148*, 415−423.

(23) Verboekend, D.; Keller, T. C.; Mitchell, S.; Pérez-Ramírez, J. Hierarchical FAU- and LTA-Type Zeolites by Post-Synthetic Design: A New Generation of Highly Efficient Base Catalysts. *Adv. Funct. Mater.* **2013**, *23*, 1923−1934.

(24) Verboekend, D.; Nuttens, N.; Locus, R.; Van Aelst, J.; Verolme, P.; Groen, J. C.; Pérez-Ramírez, J.; Sels, B. F. Synthesis, character-isation, and catalytic evaluation of hierarchical faujasite zeolites: milestones, challenges, and future directions. *Chem. Soc. Rev.* **2016**, *45*, 3331−3352.

(25) Lee, S.; Kim, H.; Choi, M. Controlled decationization of X zeolite: mesopore generation within zeolite crystallites for bulky molecular adsorption and transformation. *J. Mater. Chem. A* **2013**, *1*, 12096−12102.

(26) Verboekend, D.; Vilé, G.; Pérez-Ramírez, J. Hierarchical Y and USY Zeolites Designed by Post-Synthetic Strategies. *Adv. Funct. Mater.* **2012**, *22*, 916−928.

(27) Zhan, B.; White, M. A.; Lumsden, M.; Mueller-Neuhaus, J.; Robertson, K. N.; Cameron, T. S.; Gharghouri, M. Control of Particle Size and Surface Properties of Crystals of NaX Zeolite. *Chem. Mater.* **2002**, *14*, 3636−3642.

(28) Góra-Marek, K.; Tarach, K. A.; Piwowarska, Z.; Łaniecki, M.; Chmielarz, L. Ag-loaded zeolites Y and USY as catalysts for selective ammonia oxidation. *Catal. Sci. Technol.* **2016**, *6*, 1651−1660.

(29) Nguyen, T. H.; Kim, S.; Yoon, M.; Bae, T. Hierarchical Zeolites with Amine-Functionalized Mesoporous Domains for Carbon Dioxide Capture. *ChemSusChem* **2016**, *9*, 455−461.

(30) Jiao, W. Q.; Fu, W. H.; Liang, X. M.; Wang, Y. M.; He, M. Preparation of hierarchically structured Y zeolite with low Si/Al ratio and its applications in acetalization reactions. *RSC Adv.* **2014**, *4*, 58596−58607.

(31) García-Martínez, J.; Johnson, M.; Valla, J.; Li, K.; Ying, J. Y. Mesostructured zeolite Y—high hydrothermal stability and superior FCC catalytic performance. *Catal. Sci. Technol.* **2012**, *2*, 987−994.

(32) Phung, T. K.; Carnasciali, M. M.; Finocchio, E.; Busca, G. Catalytic conversion of ethyl acetate over faujasite zeolites. *Appl. Catal., A* **2014**, *470*, 72−80.

(33) Al-Khattaf, S.; Ali, S. A.; Aitani, A. M.; Žilková, N.; Kubička, D.; Čejka, J. Recent Advances in Reactions of Alkylbenzenes Over Novel Zeolites: The Effects of Zeolite Structure and Morphology. *Catal. Rev.: Sci. Eng.* **2014**, *56*, 333−402.

(34) Li, P.; Han, Q.; Zhang, X.; Yuan, Y.; Zhang, Y.; Guo, H.; Xu, L.; Xu, L. A new insight into the reaction behaviors of side-chain alkylation of toluene with methanol over CsX. *Catal. Sci. Technol.* **2018**, *8*, 3346−3356.

(35) Lee, H.; Lee, S.; Ryoo, R.; Choi, M. Revisiting side-chain alkylation of toluene to styrene: Critical role of microporous structures in catalysts. *J. Catal.* **2019**, *373*, 25−36.

(36) Inayat, A.; Knoke, I.; Spiecker, E.; Schwieger, W. Assemblies of Mesoporous FAU-Type Zeolite Nanosheets. *Angew. Chem., Int. Ed.* **2012**, *51*, 1962−1965.

(37) Khaleel, M.; Wagner, A. J.; Mkhoyan, K. A.; Tsapatsis, M. On the Rotational Intergrowth of Hierarchical FAU/EMT Zeolites. *Angew. Chem., Int. Ed.* **2014**, *53*, 9456−9461.

(38) Awala, H.; Gilson, J.; Retoux, R.; Boullay, P.; Goupil, J.; Valtchev, V.; Mintova, S. Template-free nanosized faujasite-type zeolites. *Nat. Mater.* **2015**, *14*, 447−451.

(39) Khaleel, M.; Xu, W.; Lesch, D. A.; Tsapatsis, M. Combining Pre- and Post-Nucleation Trajectories for the Synthesis of High FAU-Content Faujasite Nanocrystals from Organic-Free Sols. *Chem. Mater.* **2016**, *28*, 4204−4213.